Single-Crystal Atomic-Layered Molybdenum Disulfide Nanobelts with High Surface Activity

Lei Yang,[†] Hao Hong,[‡] Qi Fu,[†] Yuefei Huang,[‡] Jingyu Zhang,[||] Xudong Cui,[⊥] Zhiyong Fan,[#] Kaihui Liu,*,[‡,§] and Bin Xiang*,[†,¶]

[†]Department of Materials Science & Engineering, CAS Key Lab of Materials for Energy Conversion, and [¶]Synergetic Innovation Center of Quantum Information & Quantum Physics, University of Science and Technology of China, Hefei, Anhui 230026, China, [‡]State Key Laboratory for Mesoscopic Physics, School of Physics, and [§]Collaborative Innovation Center of Quantum Matter, and Center for Nanochemistry, Peking University, Beijing 100871, China, [||]Molecular Foundry, Lawrence Berkeley National Laboratory, 1 Cyclotron Road, Berkeley, California 94720, United States, [⊥]Science and Technology on Plasma Physics Laboratory, Research Center of Laser Fusion, CAEP, Mianyang, Sichuan 621900, China, and [#]Department of Electronic and Computer Engineering, Hong Kong University of Science and Technology, Hong Kong SAR, China

ABSTRACT Nanostructured molybdenum disulfide (MoS_2) has emerged as a promising catalytic alternative to the widely used Pt in the hydrogen evolution reaction from water because it is inexpensive and earth-abundant. The central prerequisite in realizing its potential is to enhance the surface activities by increasing the concentration of metallic edge sites. However, MoS_2 thermodynamics favors the presence of a two-dimensional basal plane, and therefore, the

one-dimensional edge sites surrounding the basal plane are very limited. Herein, we report the first synthesis of single-crystal MoS_2 nanobelts with the top surface fully covered by edge sites. The nanobelt structure comprises parallel stacked atomic layers with the basal plane vertical to the substrate, and these layer edges form the top surface of the nanobelt. The surface is highly active: it optically quenches all of the indirect band gap excitons and chemically leads to a high electrocatalytic hydrogen evolution efficiency (a low onset overpotential of 170 mV for an electrocatalytic current density of 20 mA/cm^2 and a Tafel slope of 70 mV/decade).
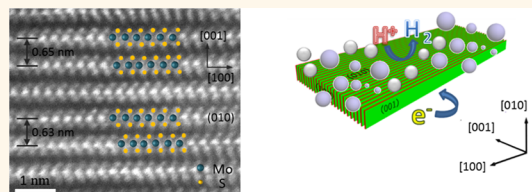
KEYWORDS: MoS_2 nanobelts · CVD · edge sites · band gap excitons · Luttinger liquid · electrocatalytic hydrogen evolution

Molybdenum disulfide (MoS_2), a rising-star atomically thin 2D material system, has attracted much research interest because of its novel electronic,[1,2] optical,[3−8] and catalytic properties.[9−18] For instance, monolayer MoS_2 exhibits a direct optical band gap of ∼1.8 eV in the visible range,[3,4] an emerging valley degree of freedom,[5−8] active metallic edge states,[19,20] and an appreciable electrocatalytic hydrogen evolution efficiency,[9−12,15,16] which are promising for novel applications in nanoelectronics,[21] photovoltaics,[22] valleytronics,[8] and industrial catalysts.[9−12,15,16] Many of these intriguing properties of MoS_2 are directly dependent on its specific atomic structure. For example, the direct band gap and valley selective circular dichroism arise in the monolayer but disappear in the 2H bilayer;[3−7] in addition, the 2D plane is semiconducting and chemically inert, whereas the plane edges are metallic and chemically

active.[19,20] Therefore, it is highly desirable to design and engineer new 2D material nanostructures to realize new functionalities and potential applications. The controls of electronic structures[12−14,23,24] and active edge sites[19,20] of 2D materials have been demonstrated as the effective means to enhance their catalytic activities.

Because MoS_2 is a van der Waals material, its most common structural configurations are two-dimensional atomic layers and three-dimensional stacked atomic layers. The one-dimensional configurations, which are energetically unfavorable, have been widely proposed theoretically[25,26] but rarely reported experimentally.[27,28] Here, we demonstrate the first successful growth of 1D single-crystal MoS_2 nanobelts using a chemical vapor deposition (CVD) method. Aberration-corrected high-resolution scanning transmission electron microscopy (STEM) reveals that these nanobelts consist of a
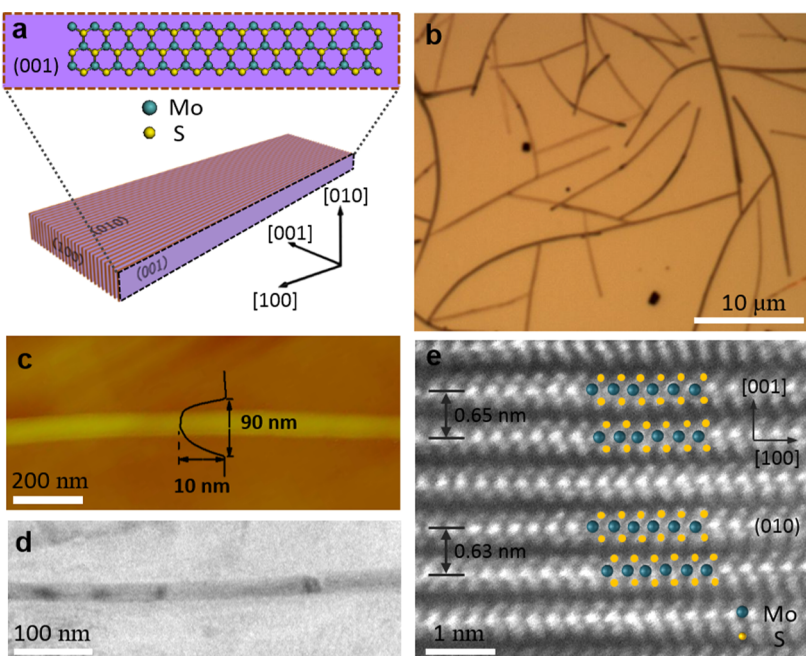
Figure 1. Morphology and crystal structure of the atomic-layered MoS$_2$ nanobelts. (a) Schematic illustration of a MoS$_2$ nanobelt. The (001) basal planes of MoS$_2$ are vertically aligned on the substrate. (b) Representative optical image of the nanobelts. The length is 10−20 μm, and the area coverage is around 5%. (c) Atomic force microscopy image of one MoS$_2$ nanobelt. The nanobelt has a width of ∼90 nm and a height of ∼10 nm. (d) Low-magnification TEM image of the MoS$_2$ nanobelt. The width is uniform along the entire nanobelt axis. (e) High-resolution STEM image of the same nanobelt as in (d). The image plane is the (010) plane, as shown in (a). The adjacent layers are 3R-like stacking (the Mo−S bond direction is the same between the adjacent layers), and the interlayer distance ranges between 0.63 and 0.65 nm, depending on the interlayer gliding along the [100] direction.

very unique structure with the base plane vertically standing on the substrates, and their top surfaces are 100% covered by the basal plane edge sites. The extreme exposing of the edge sites makes the top surface highly active, both optically and chemically. The optically generated indirect band gap excitons diffuse to the surfaces and are completely quenched by the surface states. The electrocatalytic hydrogen evolution efficiency is much higher than that of the 2D atomic layers even with an effective area coverage that is 1 order of magnitude smaller. Our results suggest the new possibility of transforming the family of 2D atomic layers into 1D nanobelt structures for electrocatalysts and other applications.

RESULTS AND DISCUSSION

Recently, 2D crystalline atomic layers of MoS$_2$ have been successfully grown using the CVD method.[29−33] To grow the 1D nanobelt structure, we developed an approach based on these previous methods but using modified growth conditions (see Methods and Supporting Information). Our key control is the use of n-type Si as the supporting substrate rather than the oxide substrates that were widely used before (the possible growth mechanism will be discussed later). The nanobelt morphology (Figure 1a, schematic drawing) was confirmed by our experimental observations. The optical image (Figure 1b) shows the long axis/width ratio (typically ∼60); the height profile

across the nanobelt of the atomic force microscopic image (Figure 1c) presents a plateau (with height of ∼10 nm and width of ∼90 nm); low-magnification transmission electron microscopy (TEM) images (Figure 1d and Supporting Information Figure S1) present obvious belt features. Our nanobelts have a length of 10−20 μm, a width of 30−500 nm, a height of 5−50 nm, and the width/height ratio centered at 8 (Supporting Information Figures S2 and S3).

To further get more detailed structural information on nanobelts at the atomic level, we employed aberration-corrected high-resolution STEM (JEOL ARM-200F) to characterize them with typical image presented in Figure 1e. Notably, the (001) basal planes are vertically standing on the substrate (Figure 1a), instead of laying on the substrate, which is the common situation observed in the growth of 2D atomic-layered materials.[29−33] The (001) planes are parallel to each other and together constitute the nanobelt structure. The edges of the base planes form the top (010) surfaces and side (100) surfaces in the nanobelt. Upon detailed examination of the nanobelt atomic structures (Figure 1e), we further observed that adjacent layers are stacked in a rhombohedral (3R)-like manner (where the Mo−S bond direction is the same between the adjacent layers), which is contrary to the prevailing hexagonal (2H)-like stacking (where the Mo−S bond direction is opposite between the adjacent layers) observed in natural minerals.[3,4]
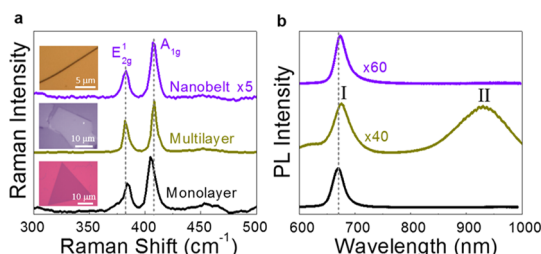
Figure 2. Optical spectra of MoS$_2$ nanobelts. (a) Representative Raman and (b) photoluminescence (PL) spectra of the nanobelt, an exfoliated multilayer, and a CVD-grown monolayer. The Raman modes of the nanobelt behave similarly to the multilayer, whereas the PL spectrum of the nanobelt exhibits distinct behavior compared with the multilayer, with the absence of the indirect band gap peak II at approximately 930 nm for the nanobelt.

We also observed that the interlayer distance is position-dependent. As guided by the cartoon spheres in Figure 1e, the two layers glide from the natural 3R bilayer structure (lower part in the image; S atoms in one layer sit on the Mo atoms of the other layer in the [001] direction) to approximately 0.12 nm along the [100] direction (top part in the image), and the interlayer distance increases from 0.63 to 0.65 nm.

Because the top surface of nanobelts is composed of the basal plane edges, in contrast to the basal plane in 2D atomic-layered materials, one may predict that the nanobelts would exhibit distinct properties. We first probed the vibrational properties of the nanobelts using Raman spectroscopy. The Raman spectra in the range of 300−500 cm^{-1} from a nanobelt, an exfoliated multilayer, and a CVD-grown monolayer are compared in Figure 2a. The two prominent peaks correspond to in-plane $^1E_{2g}$ and out-of-plane A_{1g} Raman-active modes. It has been established that interlayer van der Waals coupling will soften the $^1E_{2g}$ mode and stiffen the A_{1g} mode, which causes the two peaks in the multilayer to be further apart than in the monolayer.[34] The same trend is also observed in our nanobelt, which indicates that interlayer mechanical coupling has the same amplitude between the nanobelt and exfoliated multilayer. Couplings between the mechanical vibrations and surface electronic states in nanobelts may exist. However, this coupling appears to be too weak to yield appreciable effects in Raman spectra.

We further explored the photoluminescence (PL) properties of our nanobelts. Figure 2b presents typical PL spectra of the nanobelt, an exfoliated multilayer, and a CVD-grown monolayer. All of the spectra are normalized by peak I at approximately 670 nm, which corresponds to the MoS$_2$ direct optical transitions at the K point in the Brillouin zone. Monolayer MoS$_2$ is a direct band gap material and therefore exhibits very strong PL intensity at peak I. The exfoliated multilayer is an indirect band gap material, and the quantum yield of photoemission at peak I decreases significantly (the intensity is approximately 1/40 of that in the

monolayer), whereas a new PL peak II at approximately 930 nm arises from the indirect band gap.[3,4] The small red shift of peak I is attributed to the interlayer electronic coupling. For the nanobelt structure, the PL intensity of peak I is as weak as that in the exfoliated multilayer, which indicates that this structure is still an indirect band gap material, consistent with our previous theory on the 3R-like MoS$_2$ structure.[35] However, it is quite unusual that peak II nearly disappears. We believe that this behavior is attributed to the non-radiative recombination of excitons (electron−hole pair) at the surface of full edge states, which are metallic and provide an effective channel for exciton decay.[19] In indirect band gap MoS$_2$ materials, the photon-induced electrons and holes will mostly decay to the valence band top and conduction band bottom, respectively, forming indirect band gap excitons. In conventional 2D atomic-layered MoS$_2$, only the boundary and defects have limited edges, which will not play an important role in the exciton decay. However, in MoS$_2$ nanobelts, the top surface is fully composed of edge states (Figure 3a). Therefore, the excitons can decay nonradiatively from the edge states, and the indirect band gap PL peak II will nearly disappear if the excitons can mostly diffuse to the surfaces (Figure 3b). Our theory (Figure 3c and Methods) based on the exciton diffusion mechanism demonstrates that the PL intensity (normalized by the nanobelt height H) obeys $I/H \propto 1-2(L_D/H)\tanh(H/2L_D)$, where L_D is the exciton diffusion length.[36,37] From this theory, we know that if the exciton diffusion length is several times larger than the nanobelt height, the PL will nearly disappear. Indeed, for all our nanobelts with a height of 5−50 nm, we never observed appreciable indirect band gap PL, from which we get a lower-bound exciton diffusion length of 100 nm.

These metallic edges at the surface of 1D nanobelts are very interesting quantum states of a Luttinger liquid[38] and may be useful for next-generation electronic devices in the physical field. The MoS$_2$ edges should also be useful in the chemistry field because these edges provide active catalytic sites for hydrogen evolution.[9] Recently, MoS$_2$ was demonstrated to be a promising catalyst in the hydrogen evolution reaction (HER); however, its performance is currently mainly limited by the density of active sites. Enhancement of the active sites has been reported using mimic molecules,[10] double-gyroid morphology,[11] 1 T metallic phases,[12] or vertically aligned films.[15] Our nanobelts with the top surface fully covered by edge sites provide another option for achieving high catalytic activity.

To evaluate the electrochemical catalytic activity, we compared the MoS$_2$ nanobelts and monolayers in catalyzed electrochemical reactions of hydrogen generation. The electrochemical measurements were performed using a three-electrode cell with a 0.5 M sulfuric acid electrolyte. Before the measurements, the
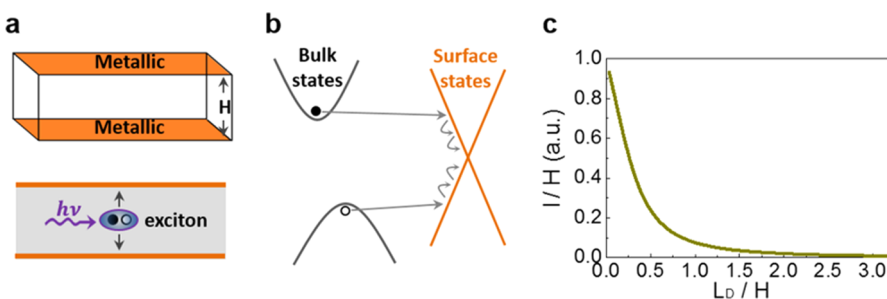
Figure 3. Mechanism for the absence of the indirect band gap PL in MoS$_2$ nanobelts. (a,b) Scheme of the structure and electronic band picture for the nanobelt. The optically induced electron hole at the band gap will first diffuse to the metallic surface and then nonradiatively decay. (c) PL intensity (I normalized by nanobelt height H) vs L_D/L, where L_D is the exciton diffusion length. When the exciton diffusion length is several times larger than the nanobelt height, the PL will be completely quenched.

electrodes were cycled several times to remove contaminant from the surface of the bare glass carbon electrode (GCE). The as-grown samples were transferred onto the bare GCE by using poly(methyl methacrylate) (PMMA) as carrier material (Figure S4, details in Supporting Information) for the HER analysis. The representative optical images in Figure S5 present the density of nanobelts and monolayers before the transfer to the GCE. Although the as-grown nanobelt area (1.5 × 0.5 mm) is one-third of the monolayer area (1.5 × 1.5 mm) and surface coverage of the nanobelts (5%) is 1/20 of the monolayer (~100%), the catalytic performance of the nanobelts is superior to that of the monolayers, as shown below.

First, the nanobelts exhibited a much lower onset overpotential (calibrated to a reversible hydrogen electrode) of 170 mV compared with 250 mV in MoS$_2$ (defined as the potential starts to generate catalytic current density of 20 mA/cm^2 as measured from the polarization plots (Figure 4b)). The catalytic current density of the nanobelt at −0.3 V vs RHE was about 10 times that of the monolayer (the current density at the same potential in our MoS$_2$ monolayers is similar to the reported value of MoS$_2$ nanosheets[12]). Second, a smaller Tafel slope of 70 mV/decade was observed in the nanobelts compared with that of 90 mV/decade in the monolayers. Lower Tafel slope means a stronger enhancement of the HER rate at a constant increase of overpotential or better chemical reactivity.[16] We also measured the stability of our nanobelts in a 20 h examination of the catalytic activity at a constantly applied potential of −0.35 V and did not find any current density decrease (Supporting Information Figure S6). The high chemical reactivity and good stability in MoS$_2$ nanobelts indicate the potential in the application of hydrogen evolution from water.

Finally, we discussed the possible growth mechanism of the atomic-layered MoS$_2$ nanobelts. The key control in our nanobelt growth is the use of silicon substrates rather than the oxide substrates used previously for 2D atomic layer growth. Generally, there is a thin layer of native silicon oxide (~2 nm) on the silicon
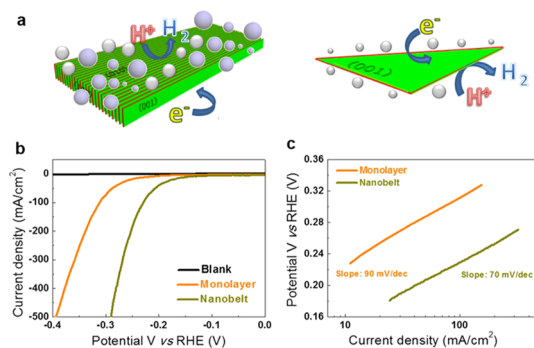
Figure 4. Electrocatalytic activity of MoS$_2$ nanobelts in hydrogen evolution. (a) Schematic illustration of electrochemical catalytic activity of the nanobelt and monolayer. The monolayer only has limited edge sites at the 2D basal plane boundaries, whereas the nanobelt has the top surface fully covered by edge sites. (b) Polarization curves of monolayer, nanobelt, and blank glass carbon electrode. The nanobelt exhibits a lower onset overpotential of 170 mV compared with that of the monolayer, 250 mV at current density of 20 mA/cm^2. (c) Tafel slopes of the monolayer and nanobelt extracted from the linear part of polarization curves (b) in logarithmic coordinates.

substrates (Resemi Company at Suzhou in China, 300 μm thick N-type ⟨100⟩ with a resistivity of 0.05−0.1 $\Omega\cdot$cm). No etching process was applied to those silicon substrates for the growth. Nanobelt structures can be also grown on 300 nm oxide substrates but with a yield 2 orders or magnitude smaller. One main difference between silicon and silicon oxide substrates is that the former has a surface energy (100 meV/Å) that is 2 orders of magnitude larger than that of the latter (2.5 meV/Å).[39,40] We assume that the high surface energy of silicon plays a key role in the growth of the MoS$_2$ nanobelts on its surface. In MoS$_2$ growth, the initial nucleation is believed to start from the formation of the MoO$_2$ structure.[32] On silicon oxide with low surface energy, MoO$_3$ prefers to form a 2D thin film structure, whereas on silicon with high surface energy, MoO$_3$ prefers to form a 3D island structure (Supporting Information Figure S7). The subsequent chemical reduction process causes a MoO$_3$ island to eventually elongate into a MoO$_2$ nanobelt structure.

Similar elongation of tungsten oxide nanoparticles during the chemical reduction has been previously reported.[41] The followed sulfurization process transforms MoO_2 into MoS_2.[32] However, the sulfurization process occurring during the MoO_2 nanobelt growth or in the end of the MoO_2 nanobelt growth still remains elusive. In our controlled experiment with shorter growth time, we observed core/shelled MoO_2/MoS_2 nanostructures (Supporting Information Figure S8), which gives the clue that the sulfurization process could occur in the end of the MoO_2 nanobelt growth. The above mechanism is one most likely growth mechanism, but we cannot exclude the others. In the future, special advanced techniques, such as *in situ* growth in TEM with real-time observation ability, can be used to study the growth mechanism in more detail.

CONCLUSIONS

In summary, we demonstrate the first growth of single-crystal atomic-layered MoS_2 nanobelts with top surfaces fully covered by active edge sites. These structures represent a family of new 1D structures from 2D transition metal dichalcogenides MX_2 (M = Mo, W; X = S, Se, Te) and may open a new pathway for optoelectronic and catalytic nanodevice applications in atomic-layered materials.

METHODS

Growth of MoS₂ Nanobelts. MoS_2 nanobelts were grown on an n-type Si substrate at atmospheric pressure using a chemical vapor deposition method in a quartz tube furnace. Before the growth, the Si substrate was sequentially cleaned in acetone, absolute ethanol, and distilled water with sonication for 10 min each. Then, the substrate was placed face-down above a boat loaded with 30 mg MoO_3, which was placed at the center of the quartz tube. The 10 mg of sulfur powder was located at the upstream side of the boat, which was 11 cm away from the center of the boat. After the system was purged with ultra-high-purity argon gas for 20 min, the furnace was heated to 650 °C at a heating rate of 15 °C/min and maintained at this temperature for 30 min; 50 sccm ultra-high-purity argon gas was used as carrier gas. After the furnace was naturally cooled to room temperature, the large-area MoS_2 nanobelts were coated on the Si substrate.

Exciton Diffusion Model. The exciton quenching in MoS_2 nanobelts can be described by exciton diffusion and dissociation at a metallic surface.[36] Excitons diffuse in MoS_2 nanobelts with the diffusion length L_D and quench when reaching the metallic top surface. Therefore, the PL intensity should be proportional to the total number of the excitons (N) in the whole nanobelts. The exciton density obeys the diffusion equation and can be written as

$$\frac{\partial^2 N}{\partial x^2} - \frac{N(x)}{L_D^2} + \frac{G_0}{L_D^2 k_0} = 0$$

where k_0 is the intrinsic decay rate and G_0 is the photon-induced exciton generation rate and is assumed to be uniform over the entire sample.[37] Considering the boundary condition

$$N(x)|_{x=0} = N(x)|_{x=H} = 0$$

we get

$$N(x) = \frac{G_0}{k_0} \frac{1}{e^{H/L_D} - \frac{H}{L_D}}[(e^{-H/L_D} - 1)e^{H/L_D}$$
$$+ (1 - e^{H/L_D})e^{-H/L_D}] + \frac{G_0}{k_0}$$

So the normalized PL intensity (by the nanobelt height H) can be expressed as

$$\frac{I}{H} \propto \frac{1}{H}\int_0^H N(x)dx = 1 - 2\frac{L_D}{H}\tanh\left(\frac{H}{2L_D}\right)$$

Electrocatalytic Measurements. All of the electrochemical experiments were conducted in a three-electrode system at room temperature with an electrochemical workstation (660E CH Instrument, Shanghai Chenhua Instrument Co., Ltd.). Before the measurements, GCE with a diameter of 3 mm was polished by α-Al_2O_3 powder (1 μm, 0.3 μm, and 50 nm) for cleaning the electrode surface. Then the electrode was washed by deionized water and ethanol and dried in air. The samples were transferred to the bare GCE with the aid of the PMMA solution method. This process is illustrated in Supporting Information Figure S4 and is similar to the procedure described under TEM sample preparation (Supporting Information Note S3). Silver paint (05002-AB, SPI Supplies) was utilized to firmly attach the sample film on the top surface of the GCE. A Ag/AgCl (3 M KCl) electrode was used as the reference electrode and a graphite rod as the counter electrode. All of the measured results are obtained after *iR* compensation, which corrects the potential drop caused by the solution resistance. Linear-sweep voltammetry with a scan rate of 5 mV/s was conducted in 0.5 M H_2SO_4. The "blank" polarization curve shown in the Figure 4b represents the catalytic performance of the bare GCE without coating MoS_2 monolayers or nanobelts.

Conflict of Interest: The authors declare no competing financial interest.

Supporting Information Available: Statistical analysis of the synthesized MoS_2 nanobelts, schematic illustration of transferring the as-grown MoS_2 nanobelts to GCE for HER, and proposed growth mechanism for MoS_2 nanobelts. The Supporting Information is available free of charge on the ACS Publications website at DOI: 10.1021/acsnano.5b02188.

REFERENCES AND NOTES

1. Radisavljevic, B.; Radenovic, A.; Brivio, J.; Giacometti, V.; Kis, A. Single-Layer MoS₂ Transistors. *Nat. Nanotechnol.* **2011**, *6*, 147–150.
2. Lopez-Sanchez, O.; Lembke, D.; Kayci, M.; Radenovic, A.; Kis, A. Ultrasensitive Photodetectors Based on Monolayer MoS₂. *Nat. Nanotechnol.* **2013**, *8*, 497–501.
3. Mak, K. K.; Lee, C.; Hone, J.; Shan, J.; Heinz, T. F. Atomically Thin MoS₂: A New Direct-Gap Semiconductor. *Phys. Rev. Lett.* **2010**, *105*, 136805.
4. Splendiani, A.; Sun, L.; Zhang, Y.; Li, T.; Kim, J.; Chim, C.-Y.; Galli, G.; Wang, F. Emerging Photoluminescence in Monolayer MoS₂. *Nano Lett.* **2010**, *10*, 1271–1275.
5. Mak, K. F.; He, K. L.; Shan, J.; Heinz, T. F. Control of Valley Polarization in Monolayer MoS₂ by Optical Helicity. *Nat. Nanotechnol.* **2012**, *7*, 494–498.
6. Zeng, H. L.; Dai, J. F.; Yao, W.; Xiao, D.; Cui, X. D. Valley Polarization in MoS₂ Monolayers by Optical Pumping. *Nat. Nanotechnol.* **2012**, *7*, 490–493.

7. Cao, T.; Wang, G.; Han, W.; Ye, H.; Zhu, C.; Shi, J.; Niu, Q.; Tan, P.; Wang, E.; Liu, B.; et al. Valley-Selective Circular Dichroism of Monolayer Molybdenum Disulphide. *Nat. Commun.* **2012**, *3*, 887.

8. Mak, K. F.; McGill, K. L.; Park, J.; McEuen, P. L. The Valley Hall Effect in MoS$_2$ Transistors. *Science* **2014**, *344*, 1489–1492.

9. Jaramillo, T. F.; Jørgensen, K. P.; Bonde, J.; Nielsen, J. H.; Horch, S.; Chorkendorff, I. Identification of Active Edge Sites for Electrochemical H$_2$ Evolution from MoS$_2$ Nanocatalysts. *Science* **2007**, *317*, 100–102.

10. Karunadasa, H. I.; Montalvo, E.; Sun, Y.; Majda, M.; Long, J. R.; Chang, C. J. A Molecular MoS$_2$ Edge Site Mimic for Catalytic Hydrogen Generation. *Science* **2012**, *335*, 698–702.

11. Kibsgaard, J.; Chen, Z.; Reinecke, B. N.; Jaramillo, T. F. Engineering the Surface Structure of MoS$_2$ To Preferentially Expose Active Edge Sites for Electrocatalysis. *Nat. Mater.* **2012**, *11*, 963–969.

12. Lukowski, M. A.; Daniel, A. S.; Meng, F.; Forticaux, A.; Li, L.; Jin, S. Enhanced Hydrogen Evolution Catalysis from Chemically Exfoliated Metallic MoS$_2$ Nanosheets. *J. Am. Chem. Soc.* **2013**, *135*, 10274–10277.

13. Voiry, D.; Salehi, M.; Silva, R.; Fujita, T.; Chen, M.; Asefa, T.; Shenoy, V. B.; Eda, G.; Chhowalla, M. Conducting MoS$_2$ Nanosheets as Catalysts for Hydrogen Evolution Reaction. *Nano Lett.* **2013**, *13*, 6222–6227.

14. Wang, H.; Lu, Z.; Xu, S.; Kong, D.; Cha, J. J.; Zheng, G.; Hsu, P.-C.; Yan, K.; Bradshaw, D.; Pritz, F. B.; et al. Electrochemical Tuning of Vertically Aligned MoS$_2$ Nanofilms and Its Application in Improving Hydrogen Evolution Reaction. *Proc. Natl. Acad. Sci. U.S.A.* **2013**, *110*, 19701–19706.

15. Kong, D.; Wang, H.; Cha, J. J.; Pasta, M.; Koski, K. J.; Yao, J.; Cui, Y. Synthesis of MoS$_2$ and MoSe$_2$ Films with Vertically Aligned Layers. *Nano Lett.* **2013**, *13*, 1341–1347.

16. Xie, J.; Zhang, H.; Li, S.; Wang, R.; Sun, X.; Zhou, M.; Zhou, J.; Lou, X. W.; Xie, Y. Defect-Rich MoS$_2$ Ultrathin Nanosheets with Additional Active Edge Sites for Enhanced Electrocatalytic Hydrogen Evolution. *Adv. Mater.* **2013**, *25*, 5807–5813.

17. Benck, J. D.; Hellstern, T. R.; Kibsgaard, J.; Chakthranont, P.; Jaramillo, T. F. Catalyzing the Hydrogen Evolution Reaction (HER) with Molybdenum Sulfide Nanomaterials. *ACS Catal.* **2014**, *4*, 3957–3971.

18. Faber, M. S.; Jin, S. Earth-Abundant Inorganic Electrocatalysts and Their Nanostructures for Energy Conversion Applications. *Energy Environ. Sci.* **2014**, *7*, 3519–3542.

19. Bollinger, M. V.; Lauritsen, J. V.; Jacobsen, K. W.; Nørskov, J. K.; Helveg, S.; Besenbacher, F. One-Dimensional Metallic Edge States in MoS$_2$. *Phys. Rev. Lett.* **2001**, *87*, 196803.

20. Yin, X.; Ye, Z.; Chenet, D. A.; Ye, Y.; O'Brien, K.; Hone, J. C.; Zhang, X. Edge Nonlinear Optics on a MoS$_2$ Atomic Monolayer. *Science* **2014**, *344*, 488–490.

21. Wang, Q. H.; Kalantar-Zadeh, K.; Kis, A.; Coleman, J. N.; Strano, M. S. Electronics and Optoelectronics of Two-Dimensional Transition Metal Dichalcogenides. *Nat. Nanotechnol.* **2012**, *7*, 699–712.

22. Feng, J.; Qian, X.; Huang, C.; Li, J. Strain-Engineered Artificial Atom as a Broad-Spectrum Solar Energy Funnel. *Nat. Photonics* **2012**, *6*, 866–872.

23. Voiry, D.; Yamaguchi, H.; Li, J.; Silva, R.; Alves, D. C. B.; Fujita, T.; Chen, M.; Asefa, T.; Shenoy, V. B.; Eda, G.; et al. Enhanced Catalytic Activity in Strained Chemically Exfoliated WS$_2$ Nanosheets for Hydrogen Evolution. *Nat. Mater.* **2013**, *12*, 850–855.

24. Lukowski, M. A.; Daniel, A. S.; English, C. R.; Meng, F.; Forticaux, A.; Hamers, R. J.; Jin, S. Highly Active Hydrogen Evolution Catalysis from Metallic WS$_2$ Nanosheets. *Energy Environ. Sci.* **2014**, *7*, 2608–2613.

25. Li, Y.; Zhou, Z.; Zhang, S.; Chen, Z. MoS$_2$ Nanoribbons: High Stability and Unusual Electronic and Magnetic Properties. *J. Am. Chem. Soc.* **2008**, *130*, 16739–16744.

26. Seivane, L. F.; Barron, H.; Botti, S.; Marques, M. A. L.; Rubio, Á.; López-Lozano, X. Atomic and Electronic Properties of Quasi-One-Dimensional MoS$_2$ Nanowires. *J. Mater. Res.* **2013**, *28*, 240–249.

27. Remskar, M.; Mrzel, A.; Skraba, Z.; Jesih, A.; Ceh, M.; Demšar, J.; Stadelmann, P.; Lévy, F.; Mihailovic, D. Self-Assembly of Subnanometer-Diameter Single-Wall MoS$_2$ Nanotubes. *Science* **2001**, *292*, 479–481.

28. Liu, X.; Xu, T.; Wu, X.; Zhang, Z.; Yu, J.; Qiu, H.; Hong, J.-H.; Jin, C.-H.; Li, J.-X.; Wang, X.-R.; et al. Top-Down Fabrication of Sub-nanometre Semiconducting Nanoribbons Derived from Molybdenum Disulfide Sheets. *Nat. Commun.* **2013**, *4*, 1776.

29. Lee, Y.-H.; Zhang, X.-Q; Zhang, W.; Chang, M.-T.; Lin, C.-T.; Chang, K.-D.; Yu, Y.-C.; Wang, J. T.-W.; Chang, C.-S.; Li, L.-L.; et al. Synthesis of Large-Area MoS$_2$ Atomic Layers with Chemical Vapor Deposition. *Adv. Mater.* **2012**, *24*, 2320–2325.

30. Zande, A. M.; Huang, P. Y.; Chenet, D. A.; Berkelbach, T. C.; You, Y.; Lee, G.-H.; Heinz, T. F.; Reichman, D. R.; Muller, D. A.; Hone, J. C. Grains and Grain Boundaries in Highly Crystalline Monolayer Molybdenum Disulphide. *Nat. Mater.* **2013**, *12*, 554–561.

31. Najmaei, S.; Liu, Z.; Zhou, W.; Zou, X.; Shi, G.; Lei, S.; Yakobson, B. I.; Idrobo, J.-C.; Ajayan, P. M.; Lou, J. Vapour Phase Growth and Grain Boundary Structure of Molybdenum Disulphide Atomic Layers. *Nat. Mater.* **2013**, *12*, 754–759.

32. Wang, X.; Feng, H.; Wu, Y.; Jiao, L. Controlled Synthesis of Highly Crystalline MoS$_2$ Flakes by Chemical Vapor Deposition. *J. Am. Chem. Soc.* **2013**, *135*, 5304–5307.

33. Tongay, S.; Fan, W.; Kang, J.; Park, J.; Koldemir, U.; Suh, J.; Narang, D. S.; Liu, K.; Ji, J.; Li, J.; et al. Tuning Interlayer Coupling in Large-Area Heterostructures with CVD-Grown MoS$_2$ and WS$_2$ Monolayers. *Nano Lett.* **2014**, *14*, 3185–3190.

34. Lee, C.; Yan, H.; Brus, L. E.; Heinz, T. F.; Hone, J.; Ryu, S. Anomalous Lattice Vibrations of Single and Few-Layer MoS$_2$. *ACS Nano* **2010**, *4*, 2695–2700.

35. Zhang, L.; Liu, K.; Wong, A. B.; Kim, J.; Hong, X.; Liu, C.; Cao, T.; Louie, S. G.; Wang, F.; Yang, P. Three-Dimensional Spirals of Atomic Layered MoS$_2$. *Nano Lett.* **2014**, *14*, 6418–6423.

36. Park, Y.; Choong, V.; Hsieh, B. R.; Tang, C. W.; Gao, Y. Gap-State Induced Photoluminescence Quenching of Phenylene Vinylene Oligomer and Its Recovery by Oxidation. *Phys. Rev. Lett.* **1997**, *78*, 3955–3958.

37. Wu, Y.; Zhou, C.; Wu, H. R.; Zhan, Y. Q.; Zhou, J.; Zhang, S. T.; Zhao, J. M.; Wang, Z. J.; Ding, X. M.; Hou, X. Y. Metal-Induced Photoluminescence Quenching of Tri-(8-hydroxyquinoline) Aluminum. *Appl. Phys. Lett.* **2005**, *87*, 044104–044106.

38. Haldane, F. D. M. Luttinger Liquid Theory of One-Dimensional Quantum Fluids: I. Properties of the Luttinger Model and Their Extension to the General 1D Interacting Spinless Fermi Gas. *J. Phys. C: Solid States Phys.* **1981**, *14*, 2585–2609.

39. Lu, G.-H.; Huang, M.; Cuma, M.; Liu, F. Relative Stability of Si Surfaces: A First-Principles Study. *Surf. Sci.* **2005**, *588*, 61–70.

40. Miskiewicz, P.; Kotarba, S.; Jung, J.; Marszalek, T.; Mas-Torrent, M.; Gomar-Nadel, E.; Amabillino, D. B.; Rovira, C.; Veciana, J.; Maniukiewicz, W.; et al. Influence of SiO$_2$ Surface Energy on the Performance of Organic Field Effect Transistors Based on Highly Oriented, Zone-Cast Layers of a Tetrathiafulvalene Derivative. *J. Appl. Phys.* **2008**, *104*, 054509.

41. Margolin, A.; Rosentsveig, R.; Albu-Yaron, A.; Popovitz-Biro, R.; Tenne, R. Study of the Growth Mechanism of WS$_2$ Nanotubes Produced by a Fluidized Bed Reactor. *J. Mater. Chem.* **2004**, *14*, 617–624.